frontiers in Neurorobotics

TYPE Original Research
PUBLISHED 02 November 2026
DOI 10.3389/fnbot.2026.1937295

Check for updates

OPEN ACCESS

EDITED BY
Jose Luis Ordoñez-Avila,
Central American Technological University, Honduras

REVIEWED BY
Ahmed Abdellatif Hamed IBRAHIM,
Arab Academy for Science, Technology and Maritime Transport (AASTMT), Egypt
Junjie Yao,
Changchun University of Chinese Medicine, China

*CORRESPONDENCE
Yi Yu
✉ 2200009@sumhs.edu.cn
Zouqin Huang
✉ hzqmusic@yeah.net
Wei Yao
✉ weiyao@fudan.edu.cn

RECEIVED 14 July 2026
REVISED 02 October 2026
ACCEPTED 05 October 2026
PUBLISHED 02 November 2026

CITATION
Zhou Y, Chen E, Lu J, Qiao X, Ren L, Yu Y, Huang Z and Yao W (2026) From biomechanical data to robotic execution: design and control of an intelligent Tuina system. *Front. Neurorobot.* 20:1937295. doi: 10.3389/fnbot.2026.1937295

COPYRIGHT
© 2026 Zhou, Chen, Lu, Qiao, Ren, Yu, Huang and Yao. This is an open-access article distributed under the terms of the Creative Commons Attribution License (CC BY). The use, distribution or reproduction in other forums is permitted, provided the original author(s) and the copyright owner(s) are credited and that the original publication in this journal is cited, in accordance with accepted academic practice. No use, distribution or reproduction is permitted which does not comply with these terms.

From biomechanical data to robotic execution: design and control of an intelligent Tuina system

Yuhui Zhou[1], Enna Chen[1], Jiale Lu[1], Xuan Qiao[1], Liujie Ren[2], Yi Yu[3]*, Zouqin Huang[4]* and Wei Yao[1,4,5]*

[1]College of Biomedical Engineering, Fudan University, Shanghai, China, [2]Eye and ENT Hospital of Fudan University, Shanghai, China, [3]College of Medical Instruments, Shanghai University of Medicine & Health Sciences, Shanghai, China, [4]Shanghai Pudong New Area Traditional Chinese Medicine Hospital, Shanghai, China, [5]Shanghai Research Center for Acupuncture and Meridian, Shanghai, China

Introduction: Traditional Chinese medicine (TCM) Tuina (massage) relies heavily on practitioners' physical stamina and subjective experience, leading to operational variability that hinders therapeutic standardization and scalable rehabilitation service delivery. To address this limitation, this study proposes an intelligent TCM Tuina robotic system integrating biomechanical data-driven design and hybrid control strategies.

Methods: A 6-DOF manipulator equipped with a biomimetic end-effector is developed, and a CMPGA-Corr neural network (Convolutional Multi-branch Prototype-Guided Architecture with a Channel-Correlation Branch) is constructed to decouple the spatiotemporal features of nine Tuina manipulations from 25-channel tactile data. Robotic execution is implemented within a Robot Operating System 2 (ROS 2)-based control framework. The framework combines RRT-Connect path planning, S-curve speed profiling, and RBF-compensated admittance control. PID, conventional Admittance, and RBF controllers were compared in complete-process simulations using five repetitions per manipulation.

Results: The RBF controller produced the lowest mean RMSE and MAE for all six evaluated manipulations. Physical experiments on a silicone back phantom further demonstrated bounded and repeatable force-tracking behavior under the tested conditions.

Discussion: The proposed framework bridges TCM practice with modern robotic engineering and provides a scalable and standardized solution for precision rehabilitation robotics.

KEYWORDS
adaptive admittance control, biomechanical data, CMPGA-Corr, force feedback, real-robot force tracking, TCM Tuina robot

1 Introduction

Tuina is a manual therapy within traditional Chinese medicine (TCM) in which practitioners use rolling, pressing, kneading, and pushing techniques to stimulate meridians, acupoints, and musculoskeletal tissues (Fang and Wand, 2021). Evidence from studies of low-back conditions supports the use of Tuina for reducing pain and improving function. A 2023 systematic review and meta-analysis of 15 randomized trials found that, compared with control interventions, Tuina significantly reduced pain and improved physical function in patients with chronic non-specific low back pain (Yang et al., 2023). In a randomized pilot study of 66 patients with lumbar disc herniation, traditional Chinese manual therapy produced greater improvements in pain, disability, and lumbar range of

motion than lumbar traction did (Cao et al., 2022). Manual Tuina delivery, however, is time-consuming and physically demanding, and may vary with a practitioner's experience and fatigue (Xu et al., 2024; Tang et al., 2025b). Robotic systems can execute prescribed trajectories and regulate contact forces while allowing an operator to define or adjust those targets (Xu et al., 2024; Tang et al., 2025b). The engineering objective is to translate practitioner-defined manipulation patterns into measurable force and motion commands for consistent and safe robotic execution.

Current robotic massage studies address several aspects of engineering execution, including platform design and task execution. A pneumatically driven soft robot and a compliant parallel manipulator illustrate two approaches to reproducing massage motions with mechanical compliance (Liu et al., 2021; Dong et al., 2023). A six-degree-of-freedom abdominal massage system further shows that one robot can implement several manual techniques while enforcing safe force limits (Tang et al., 2025a). These systems provide the mechanical basis for robotic massage. To execute a manipulation, however, a robot must also determine the correct contact location and adapt the target force to the individual. Harada et al. combined RGB-D localization with finger-force feedback to adjust position and force during massage (Harada et al., 2025). Visual-tactile fusion and acupoint detection likewise connect anatomical localization with force-position control (Yang et al., 2024; Miao and Liu, 2025). Other perception methods address narrower tasks: AIR-Net localizes hand acupoints, whereas a convolutional long short-term memory network recognizes manipulation patterns from tactile maps (Li et al., 2024; Zhu et al., 2022). After the target and technique have been defined, the controller must maintain the required force during contact. Force-sensor tracking, soft actor-critic control in simulated dynamic scenes, and online skin-model identification address this challenge through direct feedback, policy learning, and model adaptation, respectively (Harada et al., 2021; Wang et al., 2024; Zhai et al., 2022). Model-based reinforcement learning and deep reinforcement learning with variable impedance extend adaptation beyond fixed controller gains (Xiao et al., 2023; Li et al., 2024). Integrated path planning and adaptive force tracking coordinate robot motion with pressing force (Zhang et al., 2024). An impedance controller that combines gated recurrent unit prediction with online neural compensation improves the tracking of changing reference-force trajectories (Du and Xiao, 2024). Real-time assessment during massage provides additional information for updating force targets (Zhang et al., 2025). Finally, analysis of therapist motion translates expert finger-pressing profiles into robot control parameters (Harada et al., 2023). Together, this literature clarifies the roles of target localization, technique representation, motion planning, and force regulation in robotic massage. Its descriptions of expert techniques, however, usually cover only selected forces, motions, or recognized patterns (Zhu et al., 2022; Harada et al., 2023; Zhou et al., 2022; Xu Y. et al., 2024). Systematic multichannel quantification of expert Tuina manipulations remains underdeveloped. The present study addresses this need by quantifying expert manipulation patterns from multichannel tactile data, developing a new biomimetic end effector, and integrating RRT-Connect path planning, S-curve speed profiling, and radial basis function (RBF)-compensated admittance control into an intelligent TCM Tuina robot.

In this work, we develop a biomechanical data-driven model and integrate it with robotic design and adaptive control to translate expert Tuina manipulations into executable motion and force commands. To implement this approach, we record expert Tuina manipulations with a 25-channel tactile sensor, classify their spatiotemporal patterns, and execute selected techniques using a custom biomimetic end effector, trajectory planning, and adaptive force control. The Convolutional Multi-Branch Prototype-Guided Architecture with a Channel-Correlation Branch (CMPGA-Corr) decouples the spatiotemporal features of nine Tuina manipulations from these tactile data. In recording-stratified nine-fold cross-validation, the network classified the nine manipulations with a mean accuracy of 98.11%. For robotic execution, a six-degree-of-freedom (6-DOF) manipulator equipped with a custom biomimetic end effector executes six techniques: point-pressing, pressing, pushing, kneading, patting, and knocking. The control framework is implemented within Robot Operating System 2 (ROS 2) and combines RRT-Connect path planning, S-curve speed profiling, and RBF-compensated admittance control. Three controllers were compared in simulations of the complete manipulation process: a proportional-integral-derivative (PID) controller, a conventional admittance controller, and an RBF-compensated admittance controller. Across all six manipulations, the RBF-compensated controller produced the lowest mean root-mean-square error (RMSE) and mean absolute error (MAE). Normal-force tracking was then evaluated in physical experiments on a silicone back phantom. The experiments showed bounded and repeatable force-tracking behavior under the tested conditions. These results demonstrate consistent force-controlled execution of the six tested manipulations.

2 System architecture and methodology

The proposed intelligent traditional Chinese medicine (TCM) Tuina system integrates biomechanical perception, data-driven planning, adaptive force control, and robotic execution, as illustrated in Figure 1. The workflow consists of three stages. First, a 25-channel flexible tactile sensor records the force–time characteristics and spatial pressure distributions of nine clinical Tuina manipulations, and CMPGA-Corr extracts and decouples their biomechanical features. Second, camera calibration, coordinate mapping, RRT-Connect path planning, forward and inverse kinematics, and neural-network-based adaptive admittance control transform the acquired biomechanical characteristics into robot-executable trajectory and force references. Finally, a 6-DOF robotic manipulator equipped with a depth camera, biomimetic end-effector, and six-axis force/torque sensor reproduces the planned Tuina manipulations on a silicone human-back phantom.

2.1 Biomechanical data acquisition and feature extraction

2.1.1 Tactile sensing system

In the biomechanical data-acquisition stage shown in Figure 1A, a hand-shaped 25-channel flexible thin-film tactile sensor was used to record the force–time characteristics and

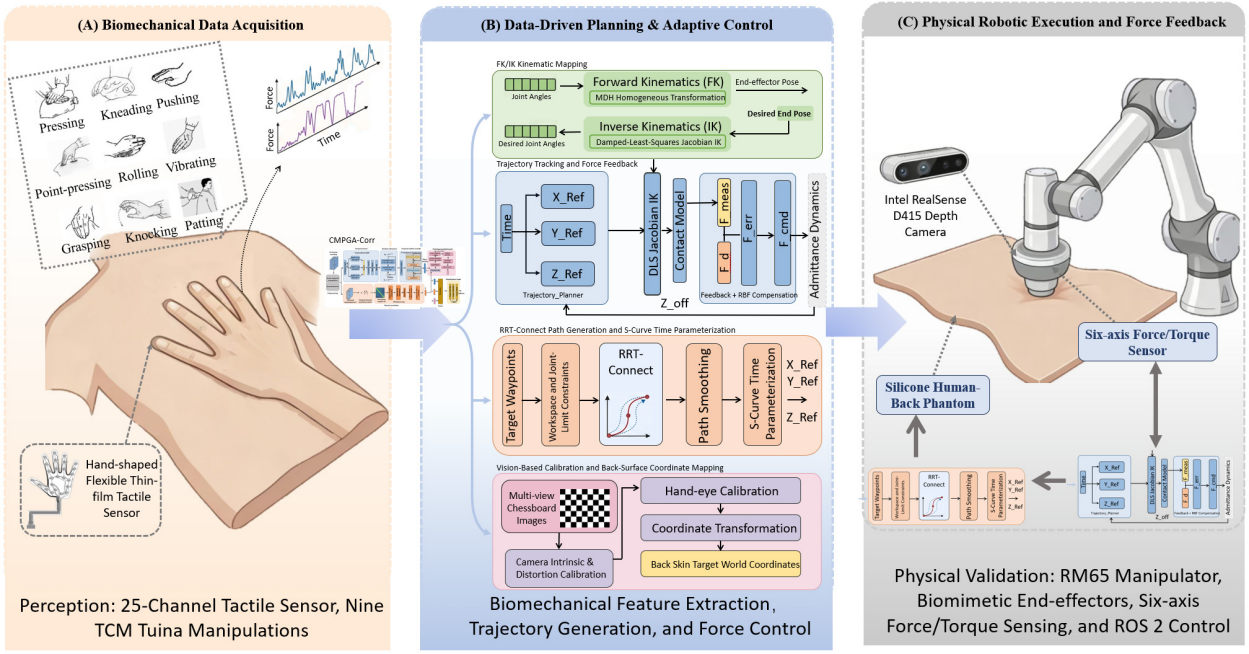

FIGURE 1
Overall framework of the proposed intelligent TCM Tuina robotic system. **(A)** Biomechanical data acquisition and feature extraction. A 25-channel hand-shaped flexible tactile sensor records the force–time characteristics and spatial pressure distributions of nine TCM Tuina manipulations, which are subsequently processed using the multi-branch CMPGA-Corr network. **(B)** Data-driven planning and control, including camera calibration, back-surface coordinate mapping, two-dimensional RRT-Connect path generation in an obstacle-free planning benchmark, S-curve time parameterization, damped-least-squares Jacobian inverse kinematics, and RBF-compensated admittance force control. **(C)** Physical robotic execution using an RM65 6-DOF manipulator, biomimetic end-effectors, an Intel RealSense D415 depth camera, and a six-axis force/torque sensor on a silicone human-back phantom. Six selected manipulations—point-pressing, pressing, pushing, kneading, patting, and knocking—were evaluated in the robotic experiments.

spatial pressure distributions of nine Tuina manipulations. Before data acquisition, a strict static three-point calibration protocol was implemented to ensure measurement accuracy. Known loads were applied using standard weights to record the raw ADC values of each channel. The system then used its built-in linear fitting algorithms to calculate and verify the gain and offset parameters, permanently storing them to ensure precise conversion from digital signals to physical pressure values. Following calibration, two certified Tuina practitioners performed nine manipulation classes on participants' backs: pressing, kneading, rolling, vibrating, patting, pushing, grasping, knocking, and point-pressing. A complete manipulation cycle, from initial contact through active force application to release, was treated as one event. The final dataset contained 900 valid events. All participants provided written informed consent before data collection.

2.1.2 CMPGA-Corr: an architecture for feature extraction

Each recording was represented as a pressure matrix. CMPGA-Corr processes this matrix through three complementary components: a temporal-context component, a channel-correlation component, and a contextual prototype-guided component. The temporal-context component uses parallel depthwise one-dimensional convolutions with kernel sizes of 3, 5, and 7, followed by an eight-head self-attention module, to model local and long-range temporal patterns. The channel-correlation component encodes pairwise statistical dependencies among the 25 sensing channels from the channel-covariance matrix. The contextual prototype-guided component introduces learnable class prototypes into the joint temporal-correlation representation. The resulting features are fused and passed to the classification head. The parallel temporal kernels provide receptive fields at different time scales, an approach that has proved effective for time-series classification (Ismail Fawaz et al., 2020). Self-attention complements the local convolutions by directly modeling long-range dependencies (Vaswani et al., 2017). The prototype-guided branch encourages samples from the same manipulation class to cluster around a class representation in the learned embedding space, following the central metric-learning principle of prototypical networks (Snell et al., 2017). In the present application, the channel-correlation branch further preserves dependencies among spatially distributed tactile channels that would be weakened by processing each channel independently.

Within-dataset performance was assessed using recording-stratified nine-fold cross-validation. Practitioner-independent generalization was assessed using two-fold leave-one-practitioner-out cross-validation, in which all events from one practitioner were held out for testing and the other practitioner's events were used for model development. Accuracy, Macro-Precision, Macro-Recall, and Macro-F1 were calculated from out-of-fold predictions.

2.2 Mechatronic implementation of the Tuina arm

As shown in Figure 2, the system integrates a robotic manipulator, an Intel RealSense D415 depth camera, custom Tuina end effectors, and a pressure sensor module. Two types of end effectors were designed to perform different Tuina techniques. The depth camera is employed to capture the surface geometry of the target region, and the pressure sensor module is used to measure contact force during the Tuina process. This integrated platform provides the hardware basis for validating the proposed perception and force-control methods.

2.2.1 Biomimetic end-effector design

The Palm-Bionic Multi-Function Effector is engineered to emulate the broad-contact maneuvers of human palm-based therapy, integrating precise actuation mechanisms to perform pressing, patting, knocking and kneading techniques with adjustable amplitude and rhythmic consistency. Conversely, the Finger-Bionic Composite Effector replicates the dexterity of digital manipulation, utilizing multi-joint articulation to execute grasping, rolling, and point-pressing stimulation with high spatial accuracy.

The proposed Finger-Bionic Composite End-Effector employs two identical planar four-bar mechanisms arranged symmetrically about the actuator centerline. The geometric relationships of the biomimetic end-effector are defined in Equations 1–11. A two-dimensional coordinate system is defined with the x-axis along the lateral opening direction and the y-axis along the vertical direction. For the left-side mechanism, the position vectors of the two fixed joints A_L and B_L are defined as

$$\mathbf{P}_{A_L} = \begin{bmatrix} -d_{offset} \\ h_A \end{bmatrix} \tag{1}$$

$$\mathbf{P}_{B_L} = \begin{bmatrix} -d_{offset} + \Delta x \\ h_B \end{bmatrix} \tag{2}$$

where Δx represents the horizontal projection of the fixed link, determined by the geometric constraint:

$$\Delta x = \sqrt{L_2^2 - \left(h_A - h_B\right)^2} \tag{3}$$

The moving links $B_L C_L$ and $A_L D_L$ have the same length L and rotate synchronously through the motor input angle θ. Accordingly, the position vector of joint C_L is

$$\mathbf{P}_{C_L}(\theta) = \mathbf{P}_{B_L} + L \begin{bmatrix} \sin\theta \\ \cos\theta \end{bmatrix} \tag{4}$$

$$\mathbf{P}_{D_L}(\theta) = \mathbf{P}_{A_L} + L \begin{bmatrix} \sin\theta \\ \cos\theta \end{bmatrix} \tag{5}$$

The coupler midpoint is defined by

$$\mathbf{M}_L(\theta) = \frac{\mathbf{P}_{C_L}(\theta) + \mathbf{P}_{D_L}(\theta)}{2} \tag{6}$$

Because the linkage constrains the terminal axis to remain aligned with the global vertical direction, the left terminal point P_L, located at a distance L_{end} above the coupler midpoint, is expressed as

$$\mathbf{P}_L(\theta) = \frac{\mathbf{P}_{D_L}(\theta) + \mathbf{P}_{C_L}(\theta)}{2} + \begin{bmatrix} 0 \\ L_{end} \end{bmatrix} \tag{7}$$

Assuming mirror symmetry between the left- and right-side mechanisms, the total aperture width is twice the horizontal distance from the left terminal point to the actuator centerline. Within the operating range considered in this study, the left terminal remains on the negative side of the centerline; therefore,

$$W(\theta) = 2\left(d_{offset} - \frac{\Delta x}{2} - L\sin\theta\right) \tag{8}$$

The vertical height of the terminal point is

$$H(\theta) = \frac{h_A + h_B}{2} + L\cos\theta + L_{\text{end}} \tag{9}$$

The aperture-width rate is

$$\dot{W}(\theta) = -2L\cos\theta\,\dot{\theta} \tag{10}$$

The terminal-height rate is

$$\dot{H}(\theta) = -L\sin\theta\,\dot{\theta} \tag{11}$$

In the analytical model and velocity calculation, θ and $\dot{\theta}$ are expressed in radians and radians per second, respectively. Angular values are converted to degrees only for presentation in Figure 3.

The kinematic characteristics of the symmetrical dual-side four-bar actuator were evaluated using MATLAB simulations, as shown in Figure 3. Over the simulated motor-angle range of $-80^\circ \le \theta \le 0^\circ$, the aperture width W decreased monotonically from approximately 16.1 cm to 8.3 cm, whereas the terminal height H increased monotonically from 16.95 cm to 20.25 cm. The resulting narrowing-and-elevation trajectory provides a coupled motion pattern suitable for reproducing lifting- and kneading-like actions in TCM Tuina.

To bridge the gap between simulation and physical reality, a 3D model was developed using SolidWorks for structural optimization. The components were then fabricated via additive manufacturing to ensure a lightweight yet robust frame. According to the technical specifications provided, the controller supports high-precision angle readback and multi-channel synchronization, allowing for the execution of complex, pre-programmed motion groups. This hardware configuration ensures that the real-world trajectory aligns precisely with the theoretical MATLAB model, providing a stable platform for therapeutic testing.

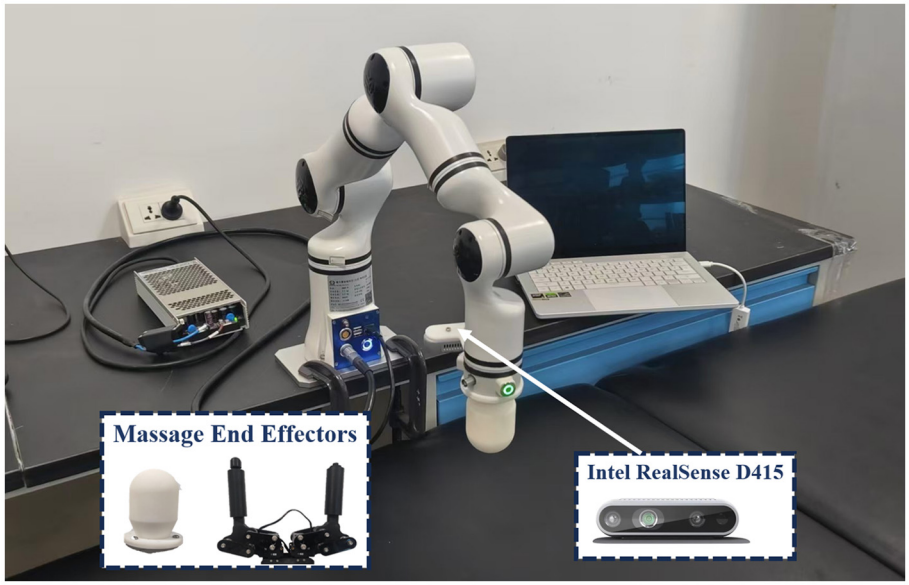

FIGURE 2
Robotic massage experimental platform. The platform consists of a robotic manipulator, custom massage end effectors, an Intel RealSense D415 depth camera, and a pressure sensor module for pose perception, contact detection, and force-feedback experiments. Specifically, the custom end effectors include a Palm-Bionic Multi-Function Effector and a Finger-Bionic Composite Effector, each designed to replicate distinct manual therapy techniques.

2.2.2 Kinematic solutions of the 6-DOF manipulator

The forward kinematics of the RM65 manipulator were formulated using the Modified Denavit–Hartenberg (MDH) convention in Equations 12–18. Let a_{i-1}, α_{i-1}, d_i, and θ_i denote the link length, link twist, joint offset, and effective joint angle, respectively. $A_i(\theta_i)$ denotes the homogeneous transform returned by the code function mdh_local with arguments α_{i-1}, a_{i-1}, d_i, and θ_i:

$$\boldsymbol{A}_i = \boldsymbol{A}\left(\theta_i; \alpha_{i-1}, a_{i-1}, d_i\right) = \begin{bmatrix} \cos\theta_i & -\sin\theta_i & 0 & a_{i-1} \\ \sin\theta_i\cos\alpha_{i-1} & \cos\theta_i\cos\alpha_{i-1} & -\sin\alpha_{i-1} & -d_i\sin\alpha_{i-1} \\ \sin\theta_i\sin\alpha_{i-1} & \cos\theta_i\sin\alpha_{i-1} & \cos\alpha_{i-1} & d_i\cos\alpha_{i-1} \\ 0 & 0 & 0 & 1 \end{bmatrix} \tag{12}$$

The joint-angle offsets implemented in the forward-kinematics code are

$$\boldsymbol{\theta}\left(\boldsymbol{q}\right) = \begin{bmatrix} q_1 \\ q_2 + \frac{\pi}{2} \\ q_3 + \frac{\pi}{2} \\ q_4 \\ q_5 \\ q_6 \end{bmatrix} \tag{13}$$

Using the parameters in Table 1, the tool pose expressed in the world frame is evaluated by the following code-equivalent matrix multiplication:

$$\boldsymbol{T}_{\mathrm{WE}}\left(\boldsymbol{q}\right) = \boldsymbol{T}_{\mathrm{base}}\left(\prod_{i=1}^{6}\boldsymbol{A}_i\right)\boldsymbol{T}_{\mathrm{tool}} \tag{14}$$

$$\boldsymbol{T}_{\mathrm{tool}} = \begin{bmatrix} \boldsymbol{I}_3 & \boldsymbol{r}_{\mathrm{tool}} \\ \boldsymbol{0}^{\mathrm{T}} & 1 \end{bmatrix} \tag{15}$$

$$\boldsymbol{r}_{\mathrm{tool}} = \begin{bmatrix} 0 \\ 0 \\ L_{\mathrm{tool}} \end{bmatrix} \tag{16}$$

$$\boldsymbol{T}_{\mathrm{WE}}(\boldsymbol{q}) = \begin{bmatrix} \boldsymbol{R}(\boldsymbol{q}) & \boldsymbol{p}(\boldsymbol{q}) \\ \boldsymbol{0}^{\mathrm{T}} & 1 \end{bmatrix} \tag{17}$$

$$\boldsymbol{p}\left(\boldsymbol{q}\right) = \begin{bmatrix} p_x\left(\boldsymbol{q}\right) \\ p_y\left(\boldsymbol{q}\right) \\ p_z\left(\boldsymbol{q}\right) \end{bmatrix} \tag{18}$$

The online simulation uses position-only damped least squares (DLS). Because the MDH geometry and Cartesian references are stored in millimeters whereas the numerical Jacobian is evaluated in meters per radian, the Cartesian position error at iteration k is

$$e_k = 10^{-3}\left[\mathbf{p}_{\mathrm{des}} - \mathbf{p}\left(\boldsymbol{q}_k\right)\right] \tag{19}$$

The translational Jacobian is obtained by finite differences. For joint j:

$$\boldsymbol{J}_{p,j}\left(\boldsymbol{q}_k\right) = 10^{-3}\frac{\boldsymbol{p}(\mathbf{q}_k+\delta\boldsymbol{\epsilon}_j)-\boldsymbol{p}(\boldsymbol{q}_k)}{\delta} \tag{20}$$

where ϵ_j is the jth Euclidean basis vector. The raw DLS increment is

10.3389/fnbot.2026.1937295

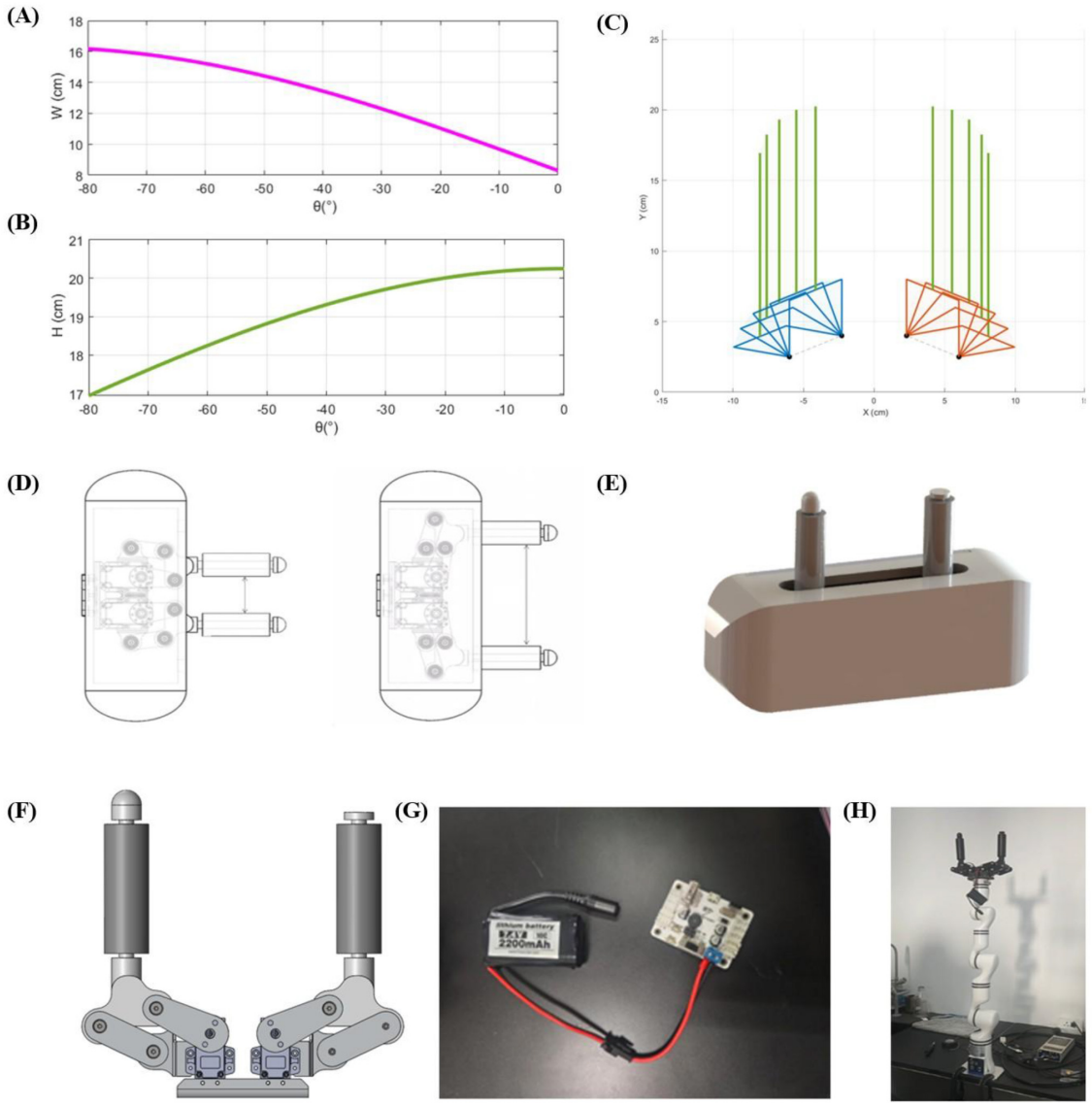

FIGURE 3
Comprehensive development workflow and kinematic characterization of the massage actuator. **(A)** Simulated relationship between motor angle and opening width; **(B)** Simulated relationship between motor angle and end-effector height; **(C)** Trajectory visualization of the four-bar linkage mechanism in MATLAB; **(D)** Technical top-view showing the variable width range in the CAD environment; **(E)** 3D rendering of the overall device housing and bionic massage heads; **(F)** Detailed structural assembly of the dual-side four-bar linkage system; **(G)** Hardware control system including the lithium battery pack and the serial bus servo controller; **(H)** Experimental platform featuring the actuator integrated onto a multi-DOF collaborative robotic arm for system-level testing.

TABLE 1 Robot structural parameters.

Joint number i	$a_{(i-1)}$ (mm)	$\alpha_{(i-1)}$ (rad)	d_i (mm)	θ_i (rad)
1	0	0	240.5	q_1
2	0	$\pi/2$	0	$q_2 + \pi/2$
3	256	0	0	$q_3 + \pi/2$
4	0	$\pi/2$	210	q_4
5	0	$-\pi/2$	0	q_5
6	0	$\pi/2$	144	q_6

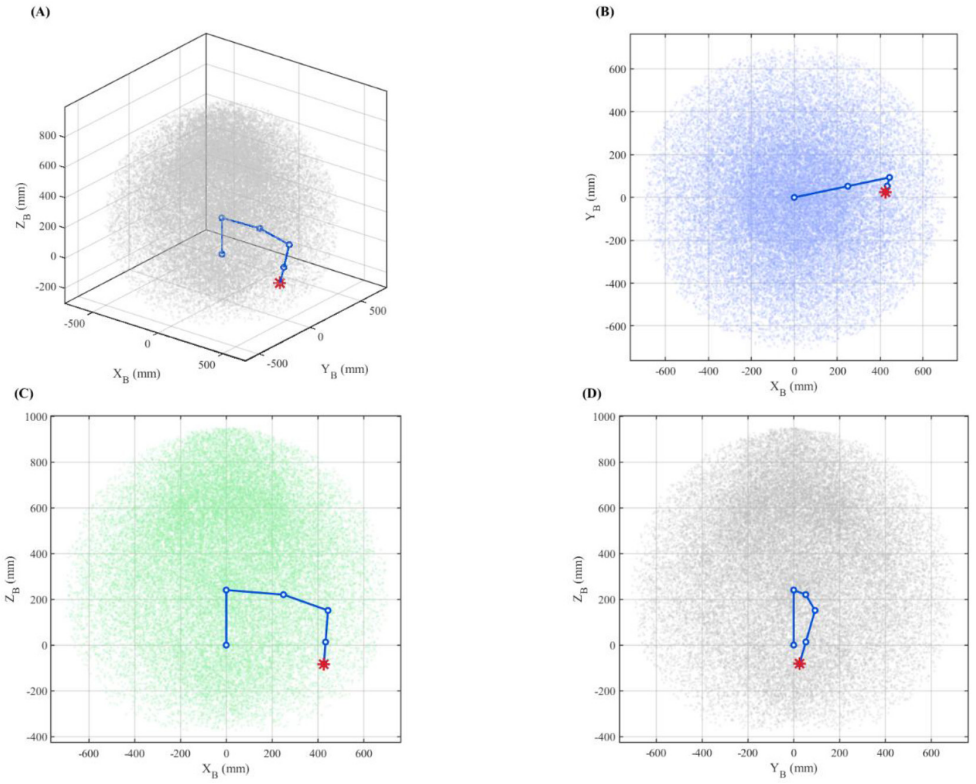

FIGURE 4
The reachable workspace of the RM65 manipulator, using the Monte Carlo random sampling technique. **(A)** 3D Workspace; **(B)** X-Y Plane; **(C)** X-Z Plane; **(D)** Y-Z Plane.

$$\Delta q_k^{\mathrm{DLS}} = \alpha J_p^{\mathrm{T}}(q_k)\left[J_p(q_k)\,J_p^{\mathrm{T}}(q_k) + \mu I_3\right]^{-1} e_{\mathbf{k}} \tag{21}$$

The damping term regularizes the Jacobian inversion near singular or ill-conditioned configurations, trading exact local inversion for bounded corrective joint motion (Wampler, 1986). The subsequent componentwise clipping provides an additional implementation-level limit on each iteration but does not replace singularity or collision analysis. In the Simulink IK_Step block, this increment is clipped componentwise before joint-limit projection:

$$\Delta q_k = \mathrm{sat}_{\Delta q\max}\left(\Delta q_k^{\mathrm{DLS}}\right) \tag{22}$$

$$q_{k+1} = \mathrm{Proj}_Q\left(q_k + \Delta q_k\right) \tag{23}$$

The numerical values were $\alpha = 0.5$ and $\mu = 10^{-3}$, with a maximum of 25 iterations and a position tolerance of $10^{-4}m$. In the complete-process MATLAB helper, the same $0.01rad$ componentwise bound is applied at the outer commanded-joint update after the numerical IK target q^* is obtained:

$$q_{\mathrm{cmd},k} = \mathrm{Proj}_Q\left\{q_{\mathrm{cmd},k-1} + \mathrm{sat}_{\Delta q\max}\left[q_k^* - q_{\mathrm{cmd},k-1}\right]\right\} \tag{24}$$

The Simulink IK_Step block and the ROS 2/Gazebo controller-comparison experiments both used the position-only DLS formulation in Equations 19–24. In these implementations, the Cartesian error satisfies $\mathbf{e}_k \in \mathbb{R}^3$, and the translational Jacobian satisfies $J_p(q_k) \in \mathbb{R}^{3\times 6}$. The finite-difference perturbation was set to $\delta = 10^{-6}$ *rad*. The maximum number of iterations was 25.

For the physical-robot experiments only, the tool orientation was additionally constrained to its pre-contact reference. The physical implementation used the weighted six-dimensional pose error. The pose-constrained inverse-kinematics and trajectory-planning formulations are given in Equations 25–30.

$$e_{\mathrm{pose},k} = \begin{bmatrix} p_d - p(q_k) \\ \eta\left[\mathrm{Log}\left(R_{\mathrm{d}}R(q_k)^{\mathrm{T}}\right)\right]^{\vee} \end{bmatrix} \in \mathbb{R}^6 \tag{25}$$

where $\eta = 0.10\ \mathrm{m\,rad^{-1}}$. The corresponding finite-difference pose Jacobian satisfies $J_{\mathrm{pose}} \in \mathbb{R}^{6\times 6}$, with $\delta = 10^{-5}$ *rad*, a step coefficient of 0.75, and a maximum of 30 iterations.

The position-reachable workspace of the RM65 manipulator was estimated using Monte Carlo sampling. The resulting reachable workspace is shown in Figure 4. A total of 100,000 joint configurations were drawn uniformly within the specified joint limits. All workspace points were expressed in the robot-base coordinate frame.

The current RBF-controlled TCP trajectory was transformed from the world frame to the robot-base frame and superimposed

on the sampled workspace. The trajectory remained within the sampled position-reachable envelope, supporting the kinematic feasibility of the evaluated massage task. The point cloud represents a Monte Carlo approximation under the specified joint limits and does not incorporate self-collision, environmental-collision, payload, torque, or prescribed-orientation constraints.

2.2.3 RRT-connect planner

A two-dimensional bidirectional RRT-Connect planner was used to generate a workspace-bounded route between adjacent target points. The bidirectional growth strategy is derived from RRT-Connect, which incrementally grows trees from the start and goal configurations toward sampled states and toward each other (Kuffner and LaValle, 2000). If x_{near} is the nearest tree node to a sampled point x_{rand}, the extension step is

$$\boldsymbol{x}_{\text{new}} = \begin{cases} \mathbf{x}_{\text{rand}}, d \le \rho, \\ \mathbf{x}_{\text{near}} + \rho \frac{\mathbf{x}_{\text{rand}} - \mathbf{x}_{\text{near}}}{d}, d > \rho, \end{cases} \tag{26}$$

$$d = \|\mathbf{x}_{\text{rand}} - \mathbf{x}_{\text{near}}\|_2 \tag{27}$$

where ρ is the extension step and ε is a small positive constant. In the current implementation, no obstacle-intersection test is applied; therefore, the planner is evaluated as an obstacle-free path-generation benchmark and is not presented as evidence of collision avoidance in a cluttered environment. After the two trees are connected, a moving-average filter is applied to each coordinate while preserving the two endpoints:

$$\bar{\boldsymbol{p}}_i = \frac{1}{|N_i|} \sum_{j \in N_i} \boldsymbol{p}_j \tag{28}$$

The smoothed polyline is subsequently traversed using a quintic time-scaling function.

$$s(\tau) = 10\tau^3 - 15\tau^4 + 6\tau^5 \tag{29}$$

Let $I_P(l)$ denote linear interpolation along the smoothed polyline at cumulative arc length l, and let L_P be its total length. The commanded Cartesian path is

$$\mathbf{p}_d(t) = I_P[s(\tau) \mathrm{L_P}] \tag{30}$$

2.3 Adaptive admittance control with RBF neural network compensation

Force regulation is performed along the local surface-normal direction. The adaptive admittance-control and RBF-compensation formulations are given in Equations 31–48. A positive control offset z_c denotes motion into the surface; in the MATLAB/Simulink coordinate convention, the commanded vertical coordinate is $z_{des} = z_{ref} - z_c$. Because the virtual stiffness used in the reported experiments was $K_a = 0$, the implemented admittance filter is a mass–damping model:

$$M_d \ddot{z}_c(t) + B_d \dot{z}_c(t) = u(t) \tag{31}$$

At discrete time k, the desired and measured normal contact forces are $F_{d,k}$ and $F_{m,k}$, respectively, and the force error is

$$e_k = F_{d,k} - F_{m,k} \tag{32}$$

A deadband is applied before feedback calculation:

$$e_k = \begin{cases} 0, |e_k| < e_{db}, \\ e_k, |e_k| \ge e_{db}. \end{cases} \tag{33}$$

$$r_k = \mathrm{sat}_{\dot{F}\max}\left(-\frac{F_{m,k} - F_{m,k-1}}{\Delta t}\right) \tag{34}$$

$$I_{k+1} = \begin{cases} \mathrm{sat}_{I\max}\left(I_k + \bar{e}_k \Delta t\right), g_{I,k} = 1 \\ \max\left(0, 1 - \rho_I \Delta t\right) I_k, g_{I,k} = 0 \end{cases} \tag{35}$$

The derivative term is a filtered negative measured-force rate. It approximates the derivative of the error during constant-reference intervals:

$$d_k = \alpha_d r_k + (1 - \alpha_d) d_{k-1} \tag{36}$$

The common PID feedback term is

$$u^{\text{raw}}_{\text{PID,k}} = K_p \bar{e}_k + K_d d_k + K_i I_k \tag{37}$$

For the RBF controller, the bounded sliding variable is constructed from the effective error and the filtered derivative term:

$$s_k = \mathrm{sat}_{s_{\max}}\left(d_k + \lambda \bar{e}_k\right) \tag{38}$$

Here $\lambda = 1s^{-1}$ in the implementation, so s_k, c_i, and b_i have units of Ns^{-1}.

The ith Gaussian basis function is

$$\phi_i(s_k) = \exp\left[-\frac{(s_k - c_i)^2}{2b_i^2}\right], i = 1, \ldots, N_h \tag{39}$$

The centers are uniformly distributed over the technique-specific interval:

$$c_i = c_{\min} + \frac{i-1}{N_h - 1}(c_{\max} - c_{\min}) \tag{40}$$

The code uses a normalized discrete weight update with leakage, conditional adaptation, and componentwise projection:

$$\hat{W}_{k+1} = \Pi_{[-W_{\max}, W_{\max}]^{N_h}} \left[\max(0, 1 - \sigma \Delta t)\, \hat{W}_k + g_k \frac{\gamma s_k \boldsymbol{\phi}(s_k) \Delta t}{1 + \boldsymbol{\phi}^T(s_k)\boldsymbol{\phi}(s_k)} \right] \quad (41)$$

where $g_k \in \{0, 1\}$ is an adaptation gate. It is one only after the technique-specific warm-up period, after sufficient contact force has been established, while the force error remains within the adaptation band, and while overshoot recovery is inactive. The RBF compensation is

$$\hat{f}_k = \mathrm{sat}_{f\,\max} \left[\hat{W}_k^{\mathrm{T}} \boldsymbol{\phi}(s_k) \right] \quad (42)$$

Thus, the uncompensated PID and Admittance baselines use $u_{PID,k}^{raw}$, whereas the proposed RBF controller uses

$$u_{\mathrm{RBF,k}}^{\mathrm{raw}} = u_{\mathrm{PID,k}}^{\mathrm{raw}} + \hat{f}_k \quad (43)$$

The technique-specific RBF-network settings, including the number of neurons, center range, Gaussian width, adaptation gain, initial weight, and leakage coefficient, are summarized in Table 2.

For each controller $c \in \{PID, Admittance, RBF\}$, command saturation and first-order filtering are then applied:

$$u_{c,k} = \alpha_u \mathrm{sat}_{u_{\max}} \left(u_{c,k}^{\mathrm{raw}} \right) + (1 - \alpha_u) u_{c,k-1} \quad (44)$$

The controller comparison differs only in how this bounded command is converted to axial velocity. The PID condition uses the static conversion

$$v_{k+1} = \mathrm{sat}_{v_{\max}} \left(\frac{u_{\mathrm{PID,k}}}{B_d} \right) \quad (45)$$

The Admittance and RBF conditions use the same mass–damping dynamics. For $K_a = 0$, the code applies the exact zero-order-hold update

$$v_{ss,k} = \frac{u_{c,k}}{B_d} \quad (46)$$

$$v_{k+1} = \mathrm{sat}_{v_{\max}} \left\{ v_{ss,k} + \left(v_k - v_{ss,k} \right) \exp\left[-\frac{B_d \Delta t}{M_d} \right] \right\} \quad (47)$$

$$z_{off,k+1} = \mathrm{sat}_{[z\min, z\max]} \left(z_{off,k} + v_{k+1} \Delta t \right) \quad (48)$$

During overshoot recovery, the integral state is reset, RBF adaptation is disabled, and a bounded retraction velocity is commanded. The controller and RBF weights are updated at 100 Hz. Weight projection, leakage, compensation saturation, velocity saturation, and offset saturation enforce implementation-level boundedness of the corresponding variables.

The force-tracking performance metrics and confidence-interval calculations are defined in Equations 49–56. In each complete run, RMSE, MAE, and overshoot were computed over the concatenated force-bearing samples. For the intermittent point-pressing, pressing, patting, and knocking manipulations, settling time and steady-state absolute error were computed for each complete contact cycle and then averaged within that run.

$$\mathrm{RMSE}_F = \sqrt{\frac{1}{N_A} \sum_{i \in A} e_i^2} \quad (49)$$

$$\mathrm{MAE}_F = \frac{1}{N_A} \sum_{i \in A} |e_i| \quad (50)$$

The absolute force overshoot was

$$M_p = \max\left\{0,\ \max_{i \in A} \left(F_{m,i} - F_{\mathrm{target}} \right) \right\} \quad (51)$$

Settling time was defined using a ±5% target-force band and a 0.10 *s* dwell requirement:

$$t_s = \min\{ t_i - t_0 \mid |e_j| \le 0.05 F_{\mathrm{target}} \} \quad (52)$$

If no sample satisfied this condition, the settling time was considered undefined. For intermittent manipulations, the run-level settling time was obtained by averaging the valid cycle-level settling times.

The steady-state absolute error was evaluated over the final 0.20*s* of the relevant force-bearing interval, denoted A_{tail}:

$$e_{\mathrm{ss,abs}} = \frac{1}{|A_{\mathrm{tail}}|} \sum_{i \in A_{\mathrm{tail}}} |e_i| \quad (53)$$

For each technique–controller condition, five complete runs were analyzed. The sample mean, sample standard deviation, and two-sided 95% Student's *t* confidence interval were calculated as

$$\bar{x} = \frac{1}{n} \sum_{r=1}^{n} x_r \quad (54)$$

$$s_x = \sqrt{\frac{1}{n-1} \sum_{r=1}^{n} (x_r - \bar{x})^2} \quad (55)$$

$$\mathrm{CI}_{95\%} = \mathrm{x} \pm \mathrm{t}_{0.975,\mathrm{n}-1} \frac{\mathrm{s_x}}{\sqrt{n}} \quad (56)$$

In the Simulink implementation shown in Figure 5, force regulation is realized through the cascaded NN_Admittance and AdmittanceDynamics blocks. The NN_Admittance block receives the desired normal force F_d, the contact force $F_m$calculated by the EnvForce block, and the sampling interval Δt. It calculates the force-tracking error $e_F = F_d - F_m$ and combines the PID feedback term with the online RBF compensation $\hat{f} = \hat{W}^T \phi(s)$ to generate the bounded command F_{cmd}. The RBF network provides additive compensation for unmodeled non-linear contact effects; it does not directly modify the prescribed virtual mass M_d, damping B_d, or other admittance parameters. The resulting F_{cmd} is

TABLE 2 Principal RBF-network parameters used for the six manipulation types.

Technique	Neurons	Center range	Width	Adaptation gain	Initial weight	Leakage
Point-pressing	35	[−60, 60]	20	0.080	0.000	1.0
Pressing	35	[−120, 120]	40	0.007	0.000	1.2
Pushing	35	[−80, 80]	25	0.005	0.010	1.0
Kneading	35	[−60, 60]	20	0.010	−0.002	1.0
Patting	25	[−30, 30]	10	0.005	0.002	2.0
Knocking	25	[−30, 30]	10	0.001	−0.015	0.5

subsequently processed by the discrete-time AdmittanceDynamics block to update the axial velocity and displacement offset z_{off}. This offset is applied to the reference z-coordinate before the damped-least-squares inverse-kinematics calculation. The updated joint configuration is propagated through the forward-kinematics and tissue-contact models, and the resulting contact force is fed back to the controller, thereby forming a closed-loop force–position regulation system for tracking both continuous and intermittent desired-force profiles.

3 System validation and performance evaluation

3.1 Biomechanical characterization

To enhance security to measurement spikes while retaining information about the upper tail of the force distribution, the 95th percentile (P95) was used as the primary force descriptor instead of the sample maximum, consistent with its use for limiting the influence of uncharacteristic spikes in interaction force/torque data (Jensen et al., 2021). In medical contact robotics, the 95th percentile of operator-applied axial force has also been used to derive a force requirement for a robotic ultrasound end-effector (Bao et al., 2021). By prioritizing P95, we ensure a balanced assessment of force control stability that avoids overfitting to rare anomalies.

The aggregated out-of-fold confusion matrix contained 883 correct predictions among 900 events. Its largest individual off-diagonal entries were 2%, and the remaining errors were distributed across several mechanically similar manipulation classes rather than being concentrated in a single class. CMPGA-Corr was compared with BiLSTM, CNN-1D, CNN-BiLSTM, MLP, ResNet1D, TCN, TimesNet, and Transformer using identical fold assignments and evaluation metrics. It achieved the highest observed mean values for all four metrics in the nine-fold evaluation (Supplementary Table S1). ResNet1D was the strongest baseline, with 97.67% Accuracy and 97.62% Macro-F1, compared with 98.11% and 98.08%, respectively, for CMPGA-Corr. Because the 0.44% accuracy difference between CMPGA-Corr and ResNet1D was not statistically distinguishable in the present sample, these results support competitive performance rather than definitive superiority. Under leave-one-practitioner-out evaluation, CMPGA-Corr also achieved the highest observed mean performance among the evaluated models (Supplementary Table S2).

Although nine manipulation types were collected to train the network, only the six most representative techniques—pressing, pushing, kneading, patting, knocking and point-pressing—were selected for validation on the physical robot.

The force-distribution characteristics of the representative manipulations are summarized in Table 3. Clear differences can be observed in both force magnitude and spatial distribution. Pressing showed the highest overall P95 force (48.26 N), whereas grasping had the highest mean force (14.90 N), indicating that these two manipulations represent different high-load mechanisms.

The dominant-region analysis further reveals distinct biomechanical signatures. Rolling, patting, pressing, kneading, pushing, and knocking were all mainly dominated by the hypothenar region, indicating that these manipulations rely heavily on palm-root or ulnar-side force transmission. By contrast, grasping and point-pressing were dominated by the thumb, while vibrating was highly concentrated in the middle finger, with a dominant share of 97.06%. These findings suggest that different massage techniques are characterized by stable and interpretable regional loading patterns.

3.2 Robotic execution and control performance

The evaluated trajectory remained within the prescribed joint limits, and the inverse-kinematics solver completed the commanded sequence without an observed solver failure. Correspondingly, Figure 6A presents the time-history of the joint angles during the operation. The curves exhibit smooth and continuous motion for all six joints, confirming that the inverse kinematics solution remains stable and within the physical joint limits throughout the massage task.

Figures 6B illustrate the force response and internal controller-state evolution in one representative simulation. The force and controller variables remained within the prescribed limits without sustained oscillation. This behavior supports bounded and empirically stable operation under the evaluated conditions.

For each technique–controller condition, five complete ROS 2/Gazebo simulation runs were conducted. Gazebo and the controller node were restarted before each run to reset the simulated system, controller states, and RBF weights. For point-pressing, pressing, patting, and knocking, RMSE, MAE, and overshoot were calculated from the concatenated force-bearing samples of each complete run. Settling time and steady-state

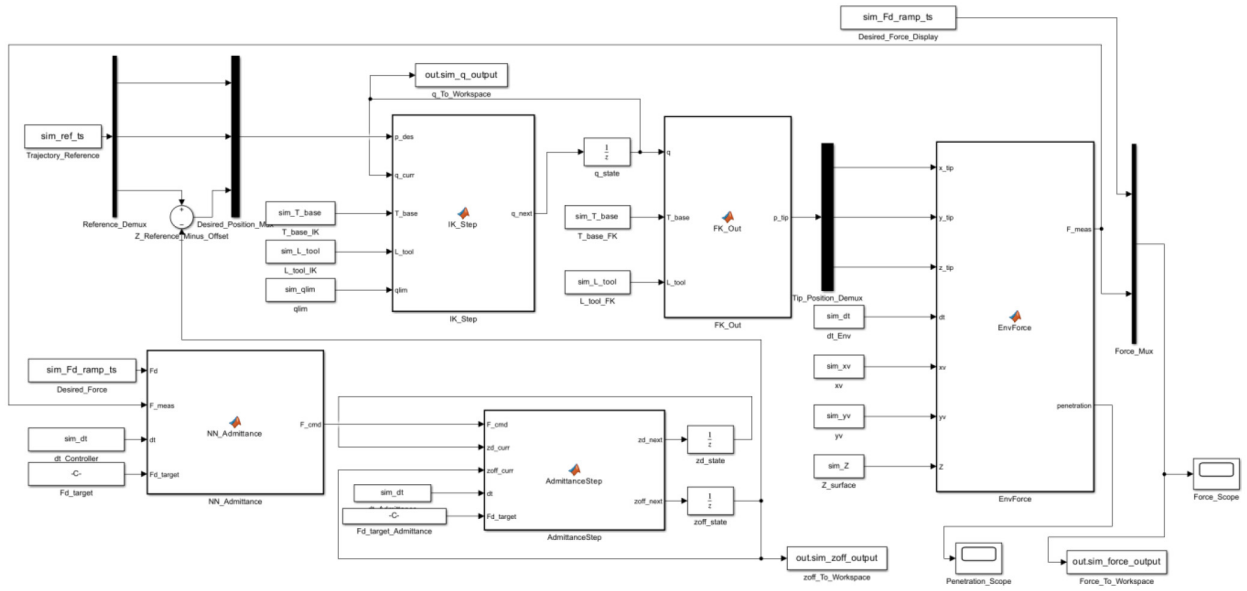

FIGURE 5
The overall control framework in the Simulink environment.

TABLE 3 The force-recognition characteristics of the nine Tuina techniques.

Technique	Mean force (N)	Overall P95 (N)	Dominant region	Dominant share (%)
Rolling	3.08	12.54	Hypothenar	46.02
Vibrating	1.86	9.41	Middle	97.06
Patting	1.26	6.23	Hypothenar	27.33
Pressing	9.99	48.26	Hypothenar	33.00
Kneading	5.70	24.56	Hypothenar	45.80
Pushing	6.73	30.96	Hypothenar	33.66
Grasping	14.90	36.09	Thumb	35.25
Knocking	2.07	9.21	Hypothenar	27.49
Point-pressing	5.63	18.76	Thumb	88.68

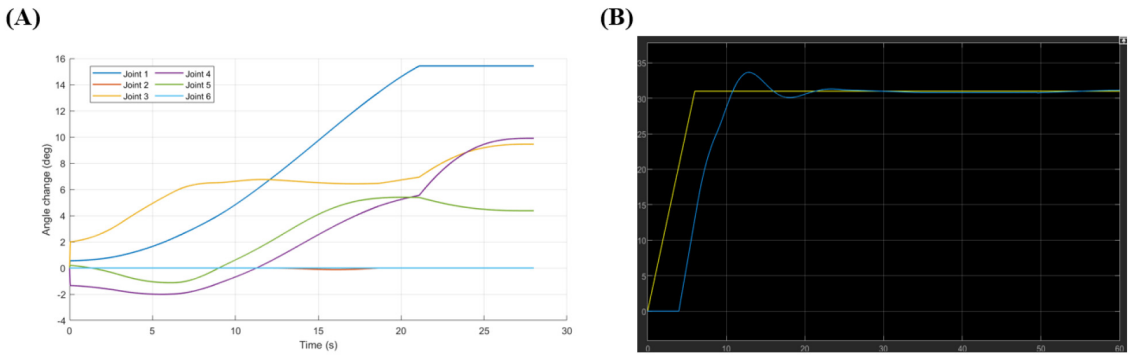

FIGURE 6
This figure illustrates the performance of the RM65 manipulator during a massage task. **(A)** Variation of the six joint angles over time during the movement; **(B)** Real-time simulation data curve generated in the Simulink Scope environment.

absolute error were calculated for each of the 10 contact cycles and then averaged within the run. Thus, the complete run, rather than an individual cycle or force sample, was treated as the statistical unit, giving five run-level observations per controller.

For each simulated technique–metric combination, the RBF controller was compared separately with PID and conventional admittance control using one-sided Welch's *t*-tests. Within each technique–metric combination, the two resulting *p*-values

were adjusted using the Holm procedure. The RBF controller significantly reduced overshoot and steady-state absolute error relative to both baselines for point-pressing. All five metrics were improved for pressing. For pushing and patting, RMSE, MAE, overshoot, and steady-state absolute error were improved. For kneading, only overshoot was significantly reduced relative to both baselines. For knocking, RMSE, MAE, and steady-state absolute error were reduced.

The RBF-compensated admittance controller produced the lowest mean RMSE and MAE for all six techniques, although the statistical evidence varied among techniques and metrics. The most consistent improvements were observed in overshoot and steady-state absolute error. For pressing, absolute overshoot decreased from 2.263 N to 1.933 N, and steady-state absolute error decreased from 1.642–1.650 N to 0.885 N. For point-pressing, overshoot decreased from 1.040–1.058 N to 0.647 N, while steady-state absolute error decreased from 0.653–0.668 N to 0.427 N. For kneading, only overshoot was significantly lower than both baselines. For knocking, all controllers exhibited zero overshoot.

Having verified the control law in the physics-based simulation, we next validated the complete system on the physical robot. This study established a physical experimental platform for the massage robot on a 6-DOF robotic manipulator (RM65) equipped with a six-axis force/torque sensor (Figure 7), with the force-tracking controller implemented under a ROS 2-based admittance control framework augmented by an RBF neural-network adaptive compensator.

Six typical Traditional Chinese Medicine (TCM) massage techniques were realized and validated on the real robot: Point-pressing (Figure 8A), Pressing (Figure 8B), Pushing (Figure 8C), Kneading (Figure 8D), Patting (Figure 8E), and Knocking (Figure 8F). For each technique, the P95 of the overall palm force obtained from practitioners was adopted as the target force threshold. This design balances therapeutic efficacy and safety by avoiding both insufficient force delivery and potential tissue injury caused by excessive loading. The measured force–time profiles of the six techniques executed on the physical robot are illustrated in Figure 8.

Point-pressing and pressing were implemented as 10 repeated contact–release cycles at fixed treatment locations. For point-pressing, the desired force was 18 N; for pressing, it was 47 N. In both cases, the measured force increased and decreased smoothly in response to the intermittent desired-force commands and returned close to zero between successive cycles.

Pushing was performed as a unidirectional approximately 80-mm surface-following motion under a 31-N force reference. Kneading combined a 24 N sustained-force reference with 10 approximately 20 mm × 14 mm elliptical motions around a fixed local treatment region. The measured kneading force remained near the prescribed level, with small fluctuations associated with motion over the curved phantom surface.

Patting and knocking were implemented as 10 intermittent low-force pulses with desired force levels of 6.5 and 9 N, respectively. Because these actions were designed as short-duration percussion-like contacts rather than sustained force plateaus, their responses were interpreted primarily using force error, peak force, release behavior, and repeatability.

To contextualize the robot-generated forces, the measured outputs were compared with previously reported expert data. The pressing force stabilized between 40 and 50 N, a range that includes the expert maximum of 42.59 N reported by Xu Y. et al. (2024). For pushing, the robot's P95 force was approximately 31 N, close to the reported expert mean of 28.94 N and below the reported maximum of 81.65 N (Xu Y. et al., 2024).

4 Discussion

The intelligent Traditional Chinese Medicine (TCM) massage system proposed in this study has achieved phased progress in addressing the standardization challenges of manual therapy by integrating biomechanical quantitative analysis with adaptive control strategies. It should be noted that the control law was first designed and verified in a high-fidelity physics-based simulation and then validated on a physical RM65 robot using a silicone back phantom; together these enable repeatable and quantitatively controllable evaluation of force–motion coupling.

At the algorithmic level, the CMPGA-Corr network effectively overcomes the feature loss inherent in traditional convolutional networks when processing long-sequence tactile signals by integrating spatiotemporal features and channel correlations. Regarding control performance, the RBF-compensated admittance controller produced lower mean values than both fixed-admittance and fixed-PID control for all non-zero and applicable metrics in the complete-process simulations. However, the strength of the statistical evidence varied among manipulation types: all five metrics were improved for pressing, pushing, and patting, whereas only selected transient or terminal metrics reached significance for point-pressing, kneading, and knocking. Within the complex curved surface environment constructed in the validation platform, the system maintains stable force output without significant overshoot or oscillation. These results indicate that the data-driven force control strategy can effectively address the challenges posed by the non-linear stiffness of human soft tissues, validating the engineering feasibility of replicating the mechanical essence described as the "coupling of rigidity and softness." However, the current experiments were performed on a silicone back phantom that does not yet fully reproduce the viscoelastic hysteresis of human skin and fascial layers, which somewhat limits the upper bound of force-control precision.

Furthermore, the force threshold setting method established in this study provides an objective basis for the safety assessment of TCM rehabilitation robots. Compared to traditional evaluation systems reliant on physicians' subjective perceptions, quantitative mechanics-based assessment criteria offer greater reproducibility. All robotic experiments were conducted on a silicone back phantom. Its geometry and mechanical response do not reproduce the heterogeneity, active responses, pain perception, or physiological variability of living tissue. Consequently, the present results demonstrate engineering feasibility and force-tracking performance only. Validation on phantoms with varied mechanical properties, formal risk assessment, and ethics-approved staged human studies are required before claims regarding safety, comfort,

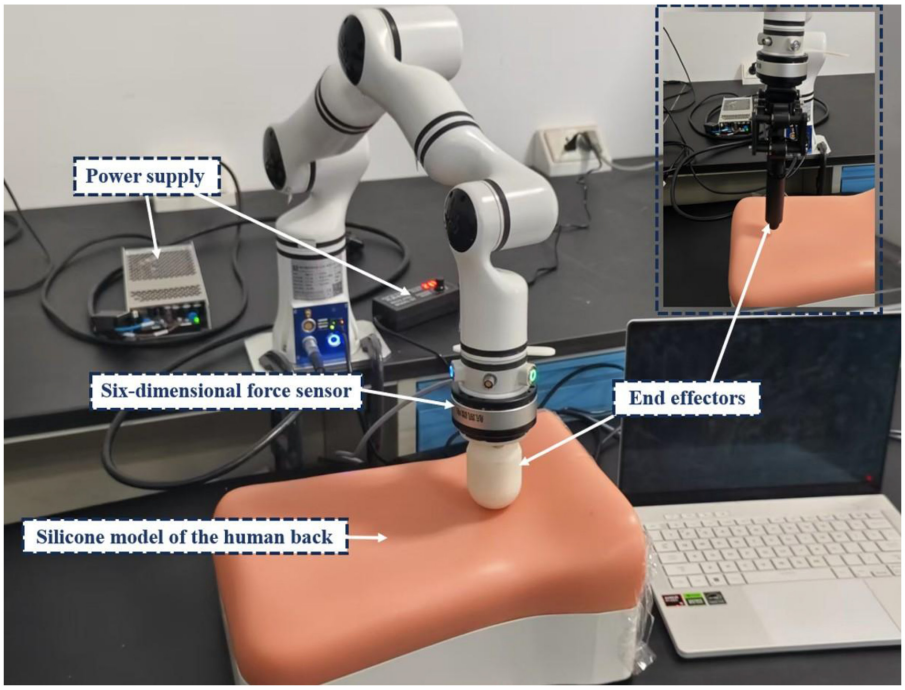

FIGURE 7
Real-robot experimental platform: a 6-DOF RM65 manipulator equipped with a six-axis force/torque sensor for force-tracking experiments.

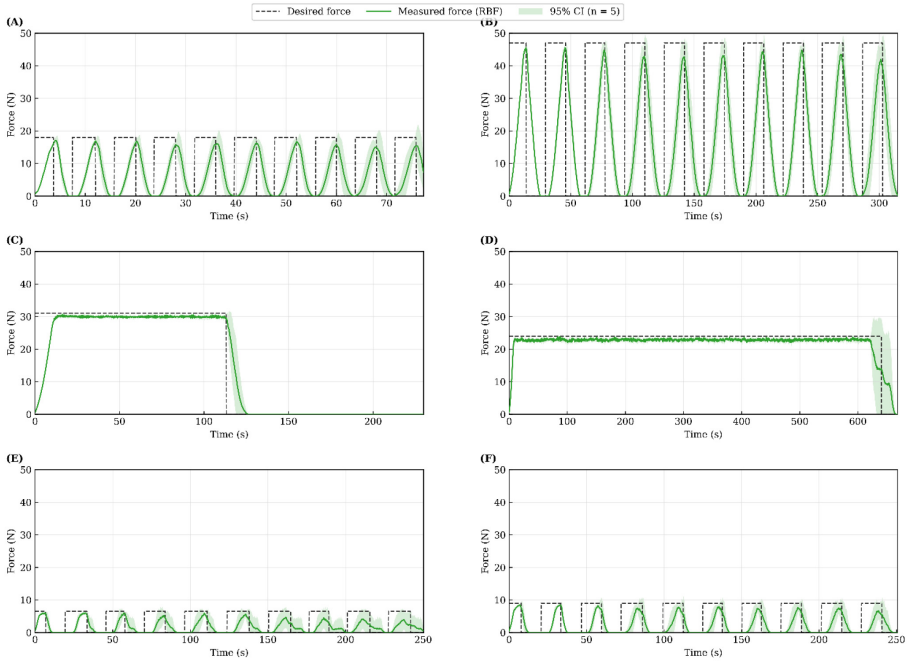

FIGURE 8
Physical-robot normal-force responses for six TCM Tuina manipulations under RBF-compensated admittance control: **(A)** point-pressing, **(B)** pressing, **(C)** pushing, **(D)** kneading, **(E)** patting, and **(F)** knocking. The black dashed line denotes the desired-force profile, whereas the green solid line represents the mean normal force measured by the six-axis force/torque sensor over five completed runs. The shaded region indssicates the two-sided 95% Student's t confidence interval ($n = 5$).

or therapeutic efficacy can be made. Future work will require higher-rate tactile sensing combined with synchronized inertial or motion-tracking measurements for impact, vibration, shear, and trajectory analysis and focus on validating the generalizability of the physical robot across diverse populations, specifically investigating adaptive parameter tuning strategies for users with

varying physiological characteristics, such as different body types and ages. Additionally, long-term operational stability tests will be conducted to ensure consistent force control performance in real-world home and community scenarios, which will be a key direction for our subsequent research.

5 Conclusions

This study successfully established an intelligent Traditional Chinese Medicine (TCM) massage system featuring a closed-loop workflow spanning from biomechanical data acquisition to robotic execution. Regarding mechatronic implementation, the design of biomimetic end-effectors and a 6-DOF manipulator effectively replicated the spatial kinematic profiles of TCM maneuvers. For control strategies, the proposed CMPGA-Corr neural network achieved high-precision recognition of manipulation categories, while the adaptive admittance control compensated by a Radial Basis Function neural network enhanced compliant interaction performance on complex curved surfaces. The simulation and physical-robot experiments demonstrated bounded and repeatable force-tracking behavior under the evaluated massage protocols. The reported results provide empirical evidence of implementation feasibility and closed-loop performance within the tested parameter and contact condition. This research confirms that data-driven massage robotics can replicate the mechanical essence of the coupling of rigidity and softness and provides a quantifiable technical pathway for the engineering and translation of TCM rehabilitation equipment.

Data availability statement

The raw data supporting the conclusions of this article will be made available by the authors, without undue reservation.

Ethics statement

The studies involving humans were approved by Shanghai Research Center for Acupuncture and Meridian. The studies were conducted in accordance with the local legislation and institutional requirements. The participants provided their written informed consent to participate in this study.

Author contributions

YZ: Methodology, Software, Writing – original draft, Validation, Conceptualization. EC: Writing – original draft, Data curation, Validation. JL: Writing – original draft, Formal analysis, Investigation, Visualization. XQ: Writing – review & editing, Resources. LR: Validation, Supervision, Writing – review & editing, Conceptualization. YY: Project administration, Writing – review & editing, Funding acquisition. ZH: Project administration, Supervision, Funding acquisition, Writing – review & editing. WY: Project administration, Writing – review & editing, Supervision, Funding acquisition.

Funding

The author(s) declared that financial support was received for this work and/or its publication. This work was supported by the National Key R&D Program of China (No. 2024YFC3505200, 2024YFC3505202), the National Natural Science Foundation of China (No. 82305416), the Shanghai Key Laboratory of Acupuncture Mechanism and Acupoint Function (No. 21DZ2271800), the Qihuang Scholars Development Program of Shanghai Pudong New Area Health Commission (No. PDZY-2026-1204), and the Famous Traditional Chinese Medicine Studio Construction Project of Shanghai Pudong New Area Health Commission (No. PDZY-2025-0707).

Conflict of interest

The author(s) declared that this work was conducted in the absence of any commercial or financial relationships that could be construed as a potential conflict of interest.

Generative AI statement

The author(s) declared that Generative AI was used in the creation of this manuscript. During the preparation of this work, the author(s) used [ChatGPT] in order to improve language and readability, check for grammatical errors and polish the text. After using this tool, the author(s) reviewed and edited the content as needed and take full responsibility for the content of the published article.

Any alternative text (alt text) provided alongside figures in this article has been generated by Frontiers with the support of artificial intelligence and reasonable efforts have been made to ensure accuracy, including review by the authors wherever possible. If you identify any issues, please contact us.

Publisher's note

All claims expressed in this article are solely those of the authors and do not necessarily represent those of their affiliated organizations, or those of the publisher, the editors and the reviewers. Any product that may be evaluated in this article, or claim that may be made by its manufacturer, is not guaranteed or endorsed by the publisher.

Supplementary material

The Supplementary Material for this article can be found online at: https://www.frontiersin.org/articles/10.3389/fnbot.2026.1937295/full#supplementary-material

References

Bao, X., Wang, S., Housden, R., Hajnal, J., and Rhode, K. (2021). A constant-force end-effector with online force adjustment for robotic ultrasonography. *IEEE Robot. Autom. Lett*. 6, 2547–2554. doi: 10.1109/LRA.2021.3061329

Cao, B., Zhou, X., Zhang, S. P., Zhu, Q. G., Kong, L. J., and Fang, M. (2022). Effect of traditional Chinese manual therapy on alleviating pain and dysfunction of lumbar disc herniation: a randomized controlled pilot study. *Am. J. Transl. Res.* 14, 6941-6952. PMID: 36398213; PMCID: PMC9641462.

Dong, H., Feng, Y., Qiu, C., and Chen, I.-M. (2023). Construction of interaction parallel manipulator: towards rehabilitation massage. *IEEE/ASME Trans. Mechatron.* 28, 372–384. doi: 10.1109/TMECH.2022.3202694

Du, L., and Xiao, M. (2024). Research on robot tracking force control algorithm based on neural networks. *Ind. Robot* 51, 1049–1056. doi: 10.1108/IR-04-2024-0176

Fang, M., and Wang, J.-G., Eds. (2021). *Tui Na Xue [Tuina Science],* 5th edn. Beijing: China Press of Traditional Chinese Medicine. ISBN: 978-7-5132-6799-1.

Harada, N., Akiduki, T., Kitazaki, M., and Tasaki, R. (2023). "Control design and implementation of robotic massage based on finger pressing motion analysis," in *2023 8th International conference on control and robotics engineering* (Niigata), 250–253. doi: 10.1109/ICCRE57112.2023.10155612

Harada, N., Kitazaki, M., and Tasaki, R. (2025). Physical therapy massage robot system with human motion tracking and finger-pressing force control. *Adv. Robot.* 39, 223–242. doi: 10.1080/01691864.2025.2469695

Harada, N., Sasakake, H., Yamashita, T., et al. (2021). "Specific muscle tracking and pressing control using force sensor in massage robot," in *Proceedings of the JSME annual conference on robotics and mechatronics 2021* (Osaka), 1A1-C11. doi: 10.1299/jsmermd.2021.1A1-C11

Ismail Fawaz, H., Lucas, B., Forestier, G., Pelletier, C., Schmidt, D. F., Weber, J., et al. (2020). InceptionTime: finding AlexNet for time series classification. *Data Min. Knowl. Discov.* 34, 1936–1962. doi: 10.1007/s10618-020-00710-y

Jensen, S. W., Salmon, J. L., and Killpack, M. D. (2021). Trends in haptic communication of human-human dyads: toward natural human-robot co-manipulation. *Front. Neurorobot.* 15:626074. doi: 10.3389/fnbot.2021.626074

Kuffner, J. J. Jr., and LaValle, S. M. (2000). "RRT-Connect: an efficient approach to single-query path planning," in *Proceedings of the 2000 IEEE International Conference on Robotics and Automation (ICRA)* (San Francisco, CA), Vol. 2, 995–1001. doi: 10.1109/ROBOT.2000.844730

Li, Y., Teng, Y., Huang, Y., Huang, L., Yang, S., Liu, J., et al. (2024). AIR-Net: acupoint image registration network for automatic acupoint recognition and localization. *Displays* 83:102743. doi: 10.1016/j.displa.2024.102743

Li, Z., Zeng, C., Deng, Z., Xu, Q., He, B., and Zhang, J. (2024). Learning variable impedance control for robotic massage with deep reinforcement learning: a novel learning framework. *IEEE Syst. Man, Cybern. Mag.* 10, 17–27. doi: 10.1109/MSMC.2022.3231416

Liu, Y., Yang, X., and Su, R. (2021). Design and modeling of a driving system for soft massage robot. *Mechatronics* 79:102640. doi: 10.1016/j.mechatronics.2021.102640

Miao, Y., and Liu, C. (2025). "An autonomous massage robot based on acupoint detection and force control strategy," in *2025 International conference on mechatronics, robotics, and artificial intelligence* (Jinan), 71–76. doi: 10.1109/MRAI65197.2025.11135874

Snell, J., Swersky, K., and Zemel, R. (2017). "Prototypical networks for few-shot learning," in *Advances in Neural Information Processing Systems* (Long Beach, CA), 30.

Tang, X., Shi, P., Luo, Z., Li, S., and Yu, H. (2025b). A study on the establishment of a variable stiffness physical model of abdominal soft tissue and an interactive massage force prediction algorithm. *Machines* 13:441. doi: 10.3390/machines13060441

Tang, X., Shi, P., Luo, Z., and Yu, H. (2025a). A novel 6-DOF multi-technique abdominal massage robot system: a new solution for relieving constipation and an exploration of standardization. *Electronics* 14:1123. doi: 10.3390/electronics14061123

Vaswani, A., Shazeer, N., Parmar, N., Uszkoreit, J., Jones, L., Gomez, A. N., et al. (2017). "Attention is all you need.," in *Advances in Neural Information Processing Systems* (Long Beach, CA), 30.

Wampler, C. W. II. (1986). Manipulator inverse kinematic solutions based on vector formulations and damped least-squares methods. *IEEE Trans. Syst. Man Cybern.* 16, 93–101. doi: 10.1109/TSMC.1986.289285

Wang, F., Chen, C., Di, C., Liu, Z., and Wang, Z. (2024). Compliance control of a rehabilitation massage robot in dynamic scenes. *J. Phys. Conf. Ser.* 2816:012103. doi: 10.1088/1742-6596/2816/1/012103

Xiao, M., Zhang, T., Zou, Y., Yan, X., and Wu, W. (2023). Study on force control for robot massage with a model-based reinforcement learning algorithm. *Intell. Serv. Robot.* 16, 509–519. doi: 10.1007/s11370-023-00474-6

Xu, Q., Deng, Z., Zeng, C., et al. (2024). Toward automatic robotic massage based on interactive trajectory planning and control. *Complex Intell. Syst.* 10, 4397–4407. doi: 10.1007/s40747-024-01384-5

Xu, Y., Huang, K., Guo, W., and Du, L. (2024). Digital modeling of massage techniques and reproduction by robotic arms. *arXiv [Preprint]*. arXiv:2412.05940.

Yang, H., Zhang, W., Si, H., and Sun, T. (2024). "Development of a massage robot based on vision-tactile fusion and adaptive force control," in *2024 6th International Conference on Robotics, Intelligent Control and Artificial Intelligence* (Nanjing), 265–269. doi: 10.1109/RICAI64321.2024.10911183

Yang, J., Zhou, X., Ma, Q., Woods, J. T., Mohabbat, A. B., Do, A., et al. (2023). Efficacy and safety of Tuina for chronic nonspecific low back pain: a PRISMA-compliant systematic review and meta-analysis. *Medicine* 102:e33018. doi: 10.1097/MD.0000000000033018

Zhai, J., Zeng, X., and Su, Z. (2022). An intelligent control system for robot massaging with uncertain skin characteristics. *Ind. Robot.* 49, 634–644. doi: 10.1108/IR-11-2021-0266

Zhang, X., Xiong, G., Yin, P., Gao, Y., and Feng, Y. (2024). Autonomous path planning and stabilizing force interaction control for robotic massage in unknown environment. *Ind. Robot* 51, 518–527. doi: 10.1108/IR-11-2023-0292

Zhang, Y., Zhang, H., Qiu, C., Xie, S., Tang, M., and Fan, Y. G. (2025). Robotic integration of massage and real-time tissue assessment: a technological framework. *IEEE Access* 13, 57910–57920. doi: 10.1109/ACCESS.2025.3549430

Zhou, Z., Wang, Y., Zhang, C., Meng, A., Hu, B., and Yu, H. (2022). Design and massaging force analysis of wearable flexible single point massager imitating traditional Chinese medicine. *Micromachines* 13:370. doi: 10.3390/mi13030370

Zhu, S., Lei, J., and Chen, D. (2022). Recognition method of massage techniques based on attention mechanism and convolutional long short-term memory neural network. *Sensors* 22:5632. doi: 10.3390/s22155632